Supporting Information for "Causes of higher climate sensitivity in CMIP6 models"

Mark D. Zelinka[1] *, Timothy A. Myers[1], Daniel T. McCoy[2], Stephen Po-Chedley[1], Peter M. Caldwell[1], Paulo Ceppi[3], Stephen A. Klein[1], and Karl E. Taylor[1]

[1]Lawrence Livermore National Laboratory, Livermore, CA, USA

[2]Institute of Climate and Atmospheric Sciences, University of Leeds, Leeds, UK

[3]Grantham Institute, Imperial College London, London, UK

Contents of this file

1. Text S1 to S6
2. Figures S1 to S11
3. Tables S1 and S2

Introduction In this Supporting Information, we provide tables of forcing, feedback, and ECS in individual CMIP5 and CMIP6 models (Tables S1 and S2), additional figures that support the results in the main text (Figures S1-S11), Text S1 explaining sensitivity to choice of radiative kernel, Texts S2 and S3 providing more information about the approximate partial radiative perturbation and Webb et al. (2006) techniques for decomposing

*7000 East Avenue, Livermore, CA

cloud feedbacks, Text S4 detailing our implementation of the Dufresne and Bony (2008) decomposition of individual contributions to ECS, Text S5 explaining how the cloud controlling factor analysis is performed, and Text S6 explaining how the cloud water phase analysis is performed.

Text S1.

Kernel Residuals

Residuals in the radiative kernel technique can arise from several sources. Discrepancies between the mean climate state and/or radiative transfer scheme of the model used to generate the kernel and the model being diagnosed is one source. The assumption that one can linearly sum radiative flux anomalies due to perturbations in individual atmospheric layers or in individual fields is also imperfect, causing additional error.

Kernel residuals are quantified by comparing the actual model-produced clear-sky feedbacks with the sum of all kernel-derived clear-sky feedbacks (Shell et al., 2008). Following Caldwell, Zelinka, Taylor, and Marvel (2016), models for which these quantities are within 15% of each other in both the longwave (LW) and shortwave (SW) are considered to have passed this clear-sky linearity test. Having estimated radiative feedbacks with the kernels of Soden et al. (2008), Shell et al. (2008), Block and Mauritsen (2013), Huang, Xia, and Tan (2017), Pendergrass, Conley, and Vitt (2018), and Smith et al. (2018), we find the greatest number of models pass this clear-sky linearity test when employing the Huang et al. (2017) kernels, so we use them throughout the paper. We stress however that the results shown in this paper are qualitatively unchanged when using any of the other kernels. Notably, while the absolute values of individual feedbacks depend on kernel, both

the inter-model spread in individual feedbacks and the CMIP5-to-CMIP6 change in the strength of individual feedbacks are essentially identical for all kernels (Figure S2).

Text S2.

Approximate Partial Radiative Perturbation (APRP) Technique

We use the approximate partial radiative perturbation (APRP) technique of Taylor et al. (2007) to separate the SW low cloud feedback into its amount and scattering components. The method approximates the atmospheric SW radiative transfer by representing the atmosphere as a single layer that scatters and absorbs SW radiation passing through it. It is assumed that absorption occurs only on the incident beam's first pass through. Atmospheric scattering and absorption parameters for this one-layer atmosphere are then derived such that the upwelling and downwelling SW radiative fluxes at the surface and TOA match those produced by the GCM. The sensitivity of the TOA SW fluxes to changes in these parameters holding all else fixed can then be estimated. Assuming that in overcast regions, non-cloud atmospheric constituents absorb and scatter the same proportion of SW radiation as they would if clouds were abruptly cleared from the scene, one can isolate the effects on TOA SW radiation from changes in cloud cover, absorption, and scattering.

Unlike changes in SW cloud radiative effect, cloud feedbacks diagnosed using APRP are due solely to cloud changes rather than to a combination of cloud and non-cloud changes. We refer to the SW cloud feedback component due to change in cloud cover as the "cloud amount" component. We combine the scattering and (much smaller) absorption components into a single "scattering" component that is very similar to the cloud optical depth component diagnosed with cloud radiative kernels (Zelinka et al., 2012, 2013, 2016).

Taylor et al. (2007) found global mean errors in SW cloud feedbacks derived with APRP that were no larger than 10% when compared with the more accurate PRP technique. We find close agreement between kernel- and APRP-derived SW cloud feedbacks in CMIP5 and CMIP6 (Figure S5).

Text S3.

Webb et al. (2006) Cloud Feedback Classification

The technique of Webb et al. (2006) compares the relative strengths of LW and SW cloud feedbacks at each grid box to infer the type(s) of cloud changes that are most likely to have caused the feedback. Every grid box is classified into one of eight categories that are defined mathematically in the caption of Figure 3 of Webb et al. (2006). For example, a location with a large positive SW cloud feedback but a near-zero LW cloud feedback would be classified as arising from fewer and/or thinner low clouds. Following Soden and Vecchi (2011), we use the adjusted- rather than unadjusted-CRE feedback as our measure of cloud feedback, and we aggregate the eight categories produced by the Webb et al. (2006) method into the two recommended by Zelinka et al. (2016): low and non-low cloud feedbacks. Low cloud feedbacks are identified where the SW component is large but the LW component is small. These are the A and E categories of Webb et al. (2006). Non-low cloud feedbacks are identified where there are large but opposing feedbacks in the SW and LW, feedbacks in the LW with no change in the SW, or LW and SW feedbacks of the same sign. These are the B, C, D, F, G, and H categories of Webb et al. (2006).

Webb et al. (2006) demonstrated a close match between the inferred cloud types causing the feedback at any given location with those derived more directly from International

Satellite Cloud Climatology Project (ISCCP) simulator output. We have also verified that low and non-low cloud feedbacks estimated in this manner agree closely with those computed using the Zelinka et al. (2016) method for the 11 models used in this study for which ISCCP simulator output is available (not shown).

Text S4.

Contributors to ECS in Each Model

Following Dufresne and Bony (2008) and Vial, Dufresne, and Bony (2013), we compute the global surface temperature change arising from the forcing and each individual feedback based on its strength relative to the Planck feedback (Figure S7). This can be thought of as the global temperature response necessary for Planck radiative damping to remove the forcing- or feedback-induced TOA imbalance. As discussed by Caldwell et al. (2016), this breakdown can be misleading for quantitatively assessing inter-model spread, so we focus on aspects that are insensitive to methodology.

Since multi-model mean forcing and non-cloud feedbacks are only slightly changed in CMIP6, the global temperature response to these is only slightly greater in CMIP6 (2.9K vs 2.7K). Cumulative temperature changes arising from non-cloud feedbacks and forcing exhibit modest inter-model spread (upward pointing triangles). Once the temperature contributions from cloud feedback are included, the spread is dramatically increased.

Text S5.

Cloud Controlling Factor Analysis

To better quantify the reasons why extratropical low cloud amount and scattering feedbacks have become more positive in CMIP6 relative to CMIP5, we utilize cloud controlling

factor (CCF) analysis, a technique that is extensively reviewed in Klein, Hall, Norris, and Pincus (2017). This analysis exploits the fact that clouds respond quickly to their environment, and hence one can decompose greenhouse warming-induced cloud changes as the product of a time-invariant sensitivity of cloud properties to individual CCFs and the change in those CCFs with climate change. Following Myers and Norris (2016), we use sea surface temperature (SST), estimated inversion strength (EIS), surface temperature advection ($Tadv$), relative humidity at 700 hPa (RH_{700}) and pressure vertical velocity at 700 hPa (ω_{700}) to explain changes in low cloud properties. The physical bases for the low cloud dependence on these five CCFs are discussed in many studies (Myers & Norris, 2016; Klein et al., 2017; Zelinka et al., 2018).

We apply the Myers and Norris (2016) analysis to anomalies in low cloud cover (LCC) and in-cloud LWP for low clouds ($\mathrm{LWP_{low}}$) in the southern extratropics (30-60°S) as follows. First, we compute deseasonalized monthly anomalies in cloud properties and cloud controlling factors at each oceanic grid box in the 30-60°S latitude band from the first 50 years of each model's piControl simulation. Anomalies in LCC and $\mathrm{LWP_{low}}$ are estimated as the total cloud cover and LWP anomalies, respectively, where the local TOA radiation anomaly is attributable to low clouds. Attribution to low clouds is performed by comparing the relative strengths of anomalies in LW and SW cloud radiative effects, defined as the clear- minus all-sky difference in upwelling TOA LW and SW radiative fluxes, respectively. This follows the same approach as is used for attributing cloud feedbacks to clouds at different altitudes (Webb et al., 2006), which is detailed in Text S3. Second, for each variable, we create a single vector of the resulting anomalies from all

grid boxes. These vectors contain a mix of spatial and temporal variability of interannual anomalies. Third, because the CCFs have different units, we normalize the CCF vectors by their current-climate spatio-temporal standard deviations taken from ERA5 ((C3S), 2017) between 1982 and 2018. (This is the reason why sensitivities are expressed in 'per σ' units and why the changes in CCFs with warming are in units of 'σ per K' in Figure 3A-D.) Finally, multiple linear regression is applied to these vectors. The resultant regression coefficients provide estimates of the dependence of low cloud properties on each of the five CCFs in the absence of confounding changes in the other four CCFs. Necessary diagnostics are not available for all models, so the sample size noted in Figure 3 is reduced relative to that of Figure 1.

Text S6.

Cloud Water Phase Analysis

Following McCoy, Hartmann, Zelinka, Ceppi, and Grosvenor (2015), we estimate the liquid condensate fraction (LCF) as a function of atmospheric temperature in each model as follows. At each atmospheric layer and for each month, we compute the ratio of liquid water mass fraction to total (liquid plus ice) water mass fraction. These liquid and ice water mass fractions, known respectively as 'clw' and 'cli' in CMIP parlance, include both large-scale and convective clouds and are the mass of cloud water divided by the mass of air (including the water in all phases) in each grid cell. Any grid cell with a total water mass fraction less than 10^{-7} kg/kg is ignored. These ratios were then averaged into bins of atmospheric temperature. Figure S10A shows the resultant LCF curves for each model providing sufficient data (which is a smaller number than

elsewhere in the paper; see sample sizes printed in the legend). The temperature at which each LCF curve intersects a value of 0.5 represents the temperature at which ice and liquid phases are present in equal proportion, and is referred to as T5050 (McCoy et al., 2015). Histograms of T5050 values are shown in Figure S10B. To assist in visualizing the CMIP5 and CMIP6 distributions, overlain are kernel density estimates that represent non-parametric inferences of the underlying probability density functions of the T5050 populations.

References

Block, K., & Mauritsen, T. (2013). Forcing and feedback in the mpi-esm-lr coupled model under abruptly quadrupled co2. *Journal of Advances in Modeling Earth Systems*, *5*(4), 676-691. doi: 10.1002/jame.20041

(C3S), C. C. C. S. (2017). ERA5: Fifth generation of ECMWF atmospheric reanalyses of the global climate. *Copernicus Climate Change Service Climate Data Store (CDS)*, *8 July 2018*. doi: https://cds.climate.copernicus.eu/cdsapp#!/home

Caldwell, P. M., Zelinka, M. D., Taylor, K. E., & Marvel, K. (2016). Quantifying the sources of intermodel spread in equilibrium climate sensitivity. *Journal of Climate*, *29*(2), 513-524. doi: 10.1175/jcli-d-15-0352.1

Dufresne, J.-L., & Bony, S. (2008). An assessment of the primary sources of spread of global warming estimates from coupled atmosphere–ocean models. *Journal of Climate*, *21*, 5135–5144. doi: 10.1175/2008JCLI2239.1

Held, I. M., & Shell, K. M. (2012). Using relative humidity as a state variable in climate feedback analysis. *Journal of Climate*, *25*(8), 2578-2582. doi: 10.1175/

JCLI-D-11-00721.1

Huang, Y., Xia, Y., & Tan, X. X. (2017). On the pattern of co2 radiative forcing and poleward energy transport. *Journal of Geophysical Research-Atmospheres*, *122*(20), 10578-10593. doi: 10.1002/2017jd027221

Klein, S. A., Hall, A., Norris, J. R., & Pincus, R. (2017). Low-cloud feedbacks from cloud-controlling factors: A review. *Surveys in Geophysics*. doi: 10.1007/s10712-017-9433-3

McCoy, D. T., Hartmann, D. L., Zelinka, M. D., Ceppi, P., & Grosvenor, D. P. (2015). Mixed-phase cloud physics and southern ocean cloud feedback in climate models. *Journal of Geophysical Research-Atmospheres*, *120*(18), 9539-9554. doi: 10.1002/2015jd023603

Myers, T. A., & Norris, J. R. (2016). Reducing the uncertainty in subtropical cloud feedback. *Geophysical Research Letters*, *43*(5), 2144-2148. doi: 10.1002/2015gl067416

Pendergrass, A. G., Conley, A., & Vitt, F. M. (2018). Surface and top-of-atmosphere radiative feedback kernels for cesm-cam5. *Earth System Science Data*, *10*(1), 317-324. doi: 10.5194/essd-10-317-2018

Shell, K. M., Kiehl, J. T., & Shields, C. A. (2008). Using the radiative kernel technique to calculate climate feedbacks in ncar's community atmospheric model. *J. Climate*, *21*(10), 2269-2282. doi: 10.1175/2007JCLI2044.1

Smith, C. J., Kramer, R. J., Myhre, G., Forster, P. M., Soden, B. J., Andrews, T., ... Watson-Parris, D. (2018). Understanding rapid adjustments to diverse forcing agents. *Geophysical Research Letters*, *45*(21), 12023-12031. doi: 10.1029/2018gl079826

Soden, B. J., & Held, I. M. (2006). An assessment of climate feedbacks in coupled ocean-atmosphere models. *J. Climate*, *19*, 3354-3360. doi: 10.1175/JCLI3799.1

Soden, B. J., Held, I. M., Colman, R., Shell, K. M., Kiehl, J. T., & Shields, C. A. (2008). Quantifying climate feedbacks using radiative kernels. *J. Climate*, *21*, 3504-3520. doi: 10.1175/2007JCLI2110.1

Soden, B. J., & Vecchi, G. A. (2011). The vertical distribution of cloud feedback in coupled ocean-atmosphere models. *Geophys. Res. Lett.*, *38*. doi: 10.1029/2011GL047632

Taylor, K. E., Crucifix, M., Braconnot, P., Hewitt, C. D., Doutriaux, C., Broccoli, A. J., ... Webb, M. J. (2007). Estimating shortwave radiative forcing and response in climate models. *J. Climate*, *20*(11), 2530-2543. doi: 10.1175/JCLI4143.1

Vial, J., Dufresne, J.-L., & Bony, S. (2013). On the interpretation of inter-model spread in cmip5 climate sensitivity estimates. *Climate Dynamics*, *41*(11-12), 3339-3362. doi: 10.1007/s00382-013-1725-9

Webb, M. J., Senior, C. A., Sexton, D. M. H., Ingram, W. J., Williams, K. D., Ringer, M. A., ... Taylor, K. E. (2006). On the contribution of local feedback mechanisms to the range of climate sensitivity in two gcm ensembles. *Climate Dyn.*, *27*, 17-38. doi: 10.1007/s00382-006-0111-2

Zelinka, M. D., Grise, K. M., Klein, S. A., Zhou, C., DeAngelis, A. M., & Christensen, M. W. (2018). Drivers of the low-cloud response to poleward jet shifts in the north pacific in observations and models. *Journal of Climate*, *31*(19), 7925-7947. doi: 10.1175/jcli-d-18-0114.1

Zelinka, M. D., Klein, S. A., & Hartmann, D. L. (2012). Computing and partitioning cloud feedbacks using cloud property histograms. part ii: Attribution to changes in cloud amount, altitude, and optical depth. *Journal of Climate*, *25*(11), 3736-3754. doi: 10.1175/JCLI-D-11-00249.1

Zelinka, M. D., Klein, S. A., Taylor, K. E., Andrews, T., Webb, M. J., Gregory, J. M., & Forster, P. M. (2013). Contributions of different cloud types to feedbacks and rapid adjustments in cmip5. *Journal of Climate*, *26*(14), 5007-5027. doi: 10.1175/jcli-d-12-00555.1

Zelinka, M. D., Zhou, C., & Klein, S. A. (2016). Insights from a refined decomposition of cloud feedbacks. *Geophysical Research Letters*, *43*(17), 9259-9269. doi: 10.1002/2016gl069917

Table S1. ECS (in K), forcing (in Wm^{-2}), and feedback values (in $Wm^{-2}K^{-1}$) for CMIP6 models. Feedbacks indicated with asterisks refer to those computed assuming constant RH following Held and Shell (2012).

MODEL	ECS	ERF_{2x}	PL (PL*)	LR (LR*)	WV (RH)	ALB	CLD (SW / LW)	NET	ERR
BCC-CSM2-MR	3.02	3.10	-3.31 (-1.95)	-0.36 (0.01)	1.67 (-0.07)	0.43	0.51 (0.16 / 0.35)	-1.03	0.04
BCC-ESM1	3.26	3.01	-3.29 (-1.94)	-0.35 (0.01)	1.66 (-0.05)	0.47	0.52 (0.02 / 0.49)	-0.92	0.07
CAMS-CSM1-0	2.29	4.17	-3.31 (-1.91)	-0.62 (-0.05)	2.01 (0.05)	0.26	-0.36 (-0.72 / 0.36)	-1.82	0.19
CESM2	5.15	3.26	-3.34 (-1.93)	-0.53 (-0.07)	1.87 (0.00)	0.41	0.96 (0.80 / 0.17)	-0.63	0.01
CESM2-WACCM	4.68	3.30	-3.34 (-1.94)	-0.54 (-0.08)	1.86 (-0.01)	0.40	1.17 (1.05 / 0.12)	-0.71	-0.25
CNRM-CM6-1	4.90	3.64	-3.29 (-1.92)	-0.42 (-0.01)	1.75 (-0.02)	0.53	0.55 (-0.02 / 0.57)	-0.74	0.13
CNRM-CM6-1-HR	4.33	3.96	-3.33 (-1.93)	-0.57 (-0.07)	1.92 (0.02)	0.40	0.54 (-0.10 / 0.64)	-0.92	0.12
CNRM-ESM2-1	4.79	2.97	-3.29 (-1.91)	-0.47 (-0.04)	1.83 (0.01)	0.51	0.56 (0.03 / 0.53)	-0.62	0.24
CanESM5	5.64	3.68	-3.33 (-1.94)	-0.61 (-0.10)	1.97 (0.07)	0.47	0.80 (-0.02 / 0.82)	-0.65	0.03
E3SM-1-0	5.31	3.33	-3.33 (-1.92)	-0.54 (-0.10)	1.86 (0.01)	0.34	0.94 (0.75 / 0.18)	-0.63	0.11
EC-Earth3	4.10	3.31	-3.24 (-1.87)	-0.22 (0.03)	1.72 (0.10)	0.58	0.29 (0.03 / 0.26)	-0.81	0.08
EC-Earth3-Veg	4.33	3.37	-3.26 (-1.89)	-0.20 (0.04)	1.73 (0.11)	0.60	0.29 (0.02 / 0.27)	-0.78	0.07
FGOALS-f3-L	2.98	4.17	-3.20 (-1.88)	-0.37 (0.01)	1.65 (-0.05)	0.40	-0.01 (-0.21 / 0.20)	-1.40	0.14
GFDL-CM4	3.89	3.19	-3.24 (-1.89)	-0.53 (-0.07)	1.84 (0.03)	0.55	0.56 (0.03 / 0.53)	-0.82	-0.00
GISS-E2-1-G	2.71	3.94	-3.25 (-1.87)	-1.03 (-0.21)	2.19 (-0.01)	0.27	0.00 (-0.64 / 0.64)	-1.45	0.37
GISS-E2-1-H	3.12	3.53	-3.22 (-1.89)	-0.55 (-0.03)	1.91 (0.06)	0.48	-0.03 (-0.53 / 0.50)	-1.13	0.27
HadGEM3-GC31-LL	5.55	3.49	-3.27 (-1.91)	-0.41 (-0.03)	1.68 (-0.07)	0.41	0.79 (0.98 / -0.19)	-0.63	0.18
INM-CM4-8	1.83	2.70	-3.29 (-1.95)	-0.09 (0.10)	1.61 (0.08)	0.40	-0.13 (-0.19 / 0.06)	-1.48	0.02
IPSL-CM6A-LR	4.56	3.41	-3.28 (-1.91)	-0.49 (-0.02)	1.93 (0.09)	0.49	0.38 (0.13 / 0.25)	-0.75	0.22
MIROC-ES2L	2.66	4.11	-3.31 (-1.91)	-0.70 (-0.11)	1.98 (-0.01)	0.44	-0.02 (-0.35 / 0.32)	-1.54	0.07
MIROC6	2.60	3.65	-3.34 (-1.89)	-0.64 (-0.10)	2.03 (0.05)	0.51	0.12 (-0.13 / 0.25)	-1.40	-0.10
MPI-ESM1-2-HR	2.98	3.65	-3.20 (-1.86)	-0.53 (-0.06)	1.83 (0.03)	0.42	0.20 (-0.41 / 0.61)	-1.22	0.06
MRI-ESM2-0	3.13	3.43	-3.27 (-1.92)	-0.48 (-0.03)	1.71 (-0.08)	0.60	0.38 (0.12 / 0.27)	-1.10	-0.04
NESM3	4.77	3.62	-3.16 (-1.86)	-0.66 (-0.07)	1.90 (0.03)	0.53	0.40 (-0.17 / 0.57)	-0.76	0.23
NorESM2-LM	2.56	3.44	-3.35 (-1.90)	-0.67 (-0.13)	2.03 (0.03)	0.40	0.36 (0.21 / 0.15)	-1.34	-0.10
SAM0-UNICON	3.72	3.89	-3.33 (-1.93)	-0.58 (-0.08)	1.77 (-0.13)	0.42	0.69 (0.89 / -0.20)	-1.05	-0.01
UKESM1-0-LL	5.36	3.61	-3.26 (-1.90)	-0.35 (-0.00)	1.61 (-0.10)	0.53	0.81 (0.93 / -0.12)	-0.67	-0.00
Average	3.86	3.52	-3.28 (-1.91)	-0.50 (-0.05)	1.83 (0.01)	0.45	0.42 (0.10 / 0.32)	-1.00	0.08
1-sigma	1.10	0.36	0.05 (0.03)	0.18 (0.06)	0.14 (0.06)	0.09	0.36 (0.49 / 0.26)	0.34	0.13

Table S2. As in Table S1, but for CMIP5 models.

MODEL	ECS	ERF_{2x}	PL (PL*)	LR (LR*)	WV (RH)	ALB	CLD (SW / LW)	NET	ERR
ACCESS1-0	3.85	2.95	-3.23 (-1.90)	-0.42 (-0.01)	1.77 (0.03)	0.47	0.40 (0.07 / 0.33)	-0.76	0.25
ACCESS1-3	3.55	2.88	-3.27 (-1.90)	-0.41 (-0.01)	1.74 (-0.02)	0.46	0.59 (0.48 / 0.11)	-0.81	0.09
BNU-ESM	4.04	3.72	-3.20 (-1.93)	-0.12 (0.12)	1.54 (0.03)	0.71	0.10 (-0.23 / 0.33)	-0.92	0.04
CCSM4	2.94	3.48	-3.26 (-1.94)	-0.22 (0.08)	1.58 (-0.04)	0.55	0.18 (-0.09 / 0.26)	-1.18	-0.02
CNRM-CM5	3.25	3.69	-3.26 (-1.92)	-0.32 (0.00)	1.62 (-0.04)	0.50	0.10 (-0.21 / 0.31)	-1.14	0.22
CSIRO-Mk3-6-0	4.09	2.60	-3.32 (-1.91)	-0.49 (-0.04)	1.83 (-0.03)	0.43	0.59 (0.55 / 0.04)	-0.64	0.32
CanESM2	3.70	3.81	-3.34 (-1.95)	-0.44 (-0.03)	1.87 (0.07)	0.45	0.45 (-0.29 / 0.74)	-1.03	-0.02
FGOALS-g2	3.37	2.84	-3.25 (-1.94)	-0.16 (0.10)	1.65 (0.08)	0.66	0.30 (-0.06 / 0.37)	-0.84	-0.04
FGOALS-s2	4.18	3.82	-3.26 (-1.92)	-0.39 (-0.01)	1.77 (0.06)	0.58	-0.06 (-0.42 / 0.36)	-0.91	0.44
GFDL-CM3	3.96	3.01	-3.24 (-1.87)	-0.59 (-0.10)	1.75 (-0.11)	0.47	0.83 (0.60 / 0.23)	-0.76	0.02
GFDL-ESM2G	2.43	2.99	-3.26 (-1.87)	-0.76 (-0.19)	2.02 (0.06)	0.34	0.18 (-0.40 / 0.58)	-1.23	0.25
GFDL-ESM2M	2.44	3.35	-3.25 (-1.85)	-0.84 (-0.20)	2.05 (0.02)	0.31	0.07 (-0.49 / 0.56)	-1.37	0.28
GISS-E2-H	2.31	3.82	-3.21 (-1.90)	-0.45 (-0.01)	1.80 (0.05)	0.36	-0.19 (-0.72 / 0.54)	-1.66	0.03
GISS-E2-R	2.12	3.74	-3.24 (-1.91)	-0.54 (-0.05)	1.92 (0.10)	0.28	-0.19 (-0.80 / 0.61)	-1.76	0.01
HadGEM2-ES	4.60	2.91	-3.23 (-1.89)	-0.34 (0.01)	1.73 (0.03)	0.43	0.64 (0.29 / 0.36)	-0.63	0.14
IPSL-CM5A-LR	4.13	3.10	-3.32 (-1.89)	-0.85 (-0.16)	2.15 (0.03)	0.29	1.12 (0.61 / 0.51)	-0.75	-0.14
IPSL-CM5A-MR	4.11	3.31	-3.34 (-1.89)	-0.96 (-0.20)	2.25 (0.04)	0.21	1.19 (0.62 / 0.57)	-0.80	-0.14
IPSL-CM5B-LR	2.61	2.65	-3.24 (-1.92)	-0.38 (0.04)	1.78 (0.05)	0.31	0.57 (0.35 / 0.22)	-1.02	-0.06
MIROC-ESM	4.65	4.29	-3.38 (-1.93)	-0.72 (-0.13)	2.04 (0.00)	0.55	0.61 (0.20 / 0.41)	-0.92	-0.02
MIROC5	2.72	4.15	-3.30 (-1.90)	-0.59 (-0.07)	1.96 (0.05)	0.53	-0.12 (-0.38 / 0.26)	-1.53	-0.01
MPI-ESM-LR	3.63	4.10	-3.21 (-1.85)	-0.72 (-0.11)	1.91 (-0.06)	0.47	0.36 (-0.16 / 0.51)	-1.13	0.07
MPI-ESM-MR	3.45	4.11	-3.22 (-1.85)	-0.78 (-0.14)	1.94 (-0.08)	0.42	0.40 (-0.07 / 0.47)	-1.19	0.07
MPI-ESM-P	3.46	4.26	-3.24 (-1.86)	-0.79 (-0.14)	1.97 (-0.06)	0.43	0.31 (-0.21 / 0.53)	-1.23	0.09
MRI-CGCM3	2.61	3.20	-3.30 (-1.97)	-0.27 (0.06)	1.60 (-0.06)	0.57	0.21 (0.24 / -0.03)	-1.22	-0.03
NorESM1-M	2.80	3.10	-3.23 (-1.92)	-0.17 (0.09)	1.56 (-0.01)	0.51	0.21 (-0.02 / 0.24)	-1.11	0.01
bcc-csm1-1	2.82	3.24	-3.27 (-1.95)	-0.17 (0.07)	1.50 (-0.06)	0.51	0.23 (-0.15 / 0.38)	-1.15	0.05
bcc-csm1-1-m	2.89	3.43	-3.34 (-1.96)	-0.26 (0.05)	1.63 (-0.06)	0.45	0.34 (-0.02 / 0.36)	-1.19	-0.00
inmcm4	2.08	2.97	-3.24 (-1.90)	-0.38 (-0.02)	1.68 (-0.02)	0.48	0.18 (-0.03 / 0.20)	-1.43	-0.14
Average	3.31	3.41	-3.27 (-1.91)	-0.48 (-0.04)	1.81 (0.00)	0.45	0.34 (-0.03 / 0.37)	-1.08	0.06
1-sigma	0.74	0.50	0.05 (0.03)	0.24 (0.09)	0.19 (0.05)	0.11	0.34 (0.38 / 0.18)	0.29	0.14

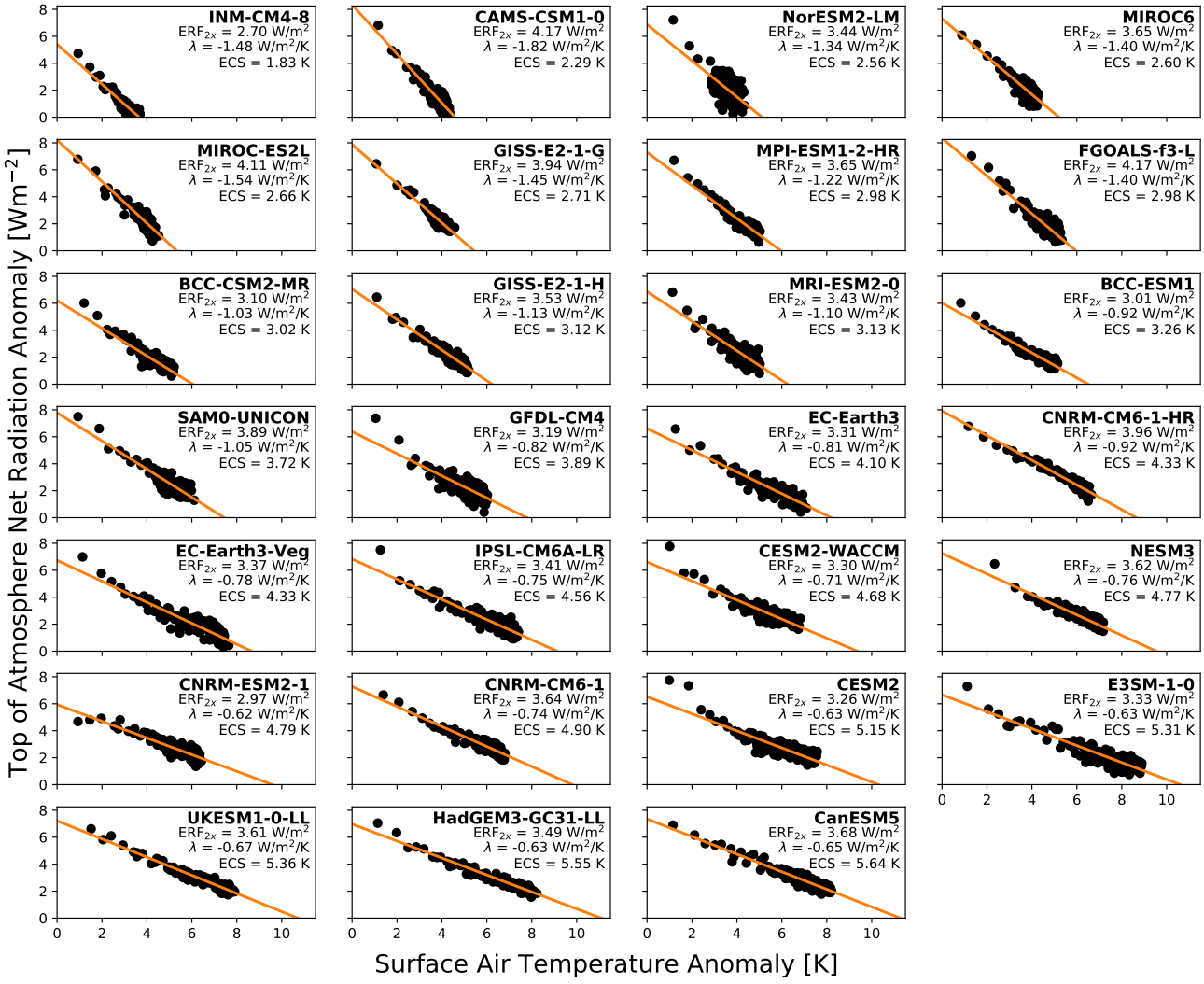

Figure S1. Gregory plots showing global and annual mean TOA net radiation anomalies plotted against global and annual mean surface air temperature anomalies. Best-fit ordinary linear least squares lines are shown. The y-intercept of the line (divided by 2) provides an estimate of the effective radiative forcing from CO_2 doubling (ERF_{2x}), the slope of the line provides an estimate of the net climate feedback parameter (λ), and the x-intercept of the line (divided by 2) provides an estimate of the effective climate sensitivity (ECS). These values are printed in each panel. Models are ordered by ECS.

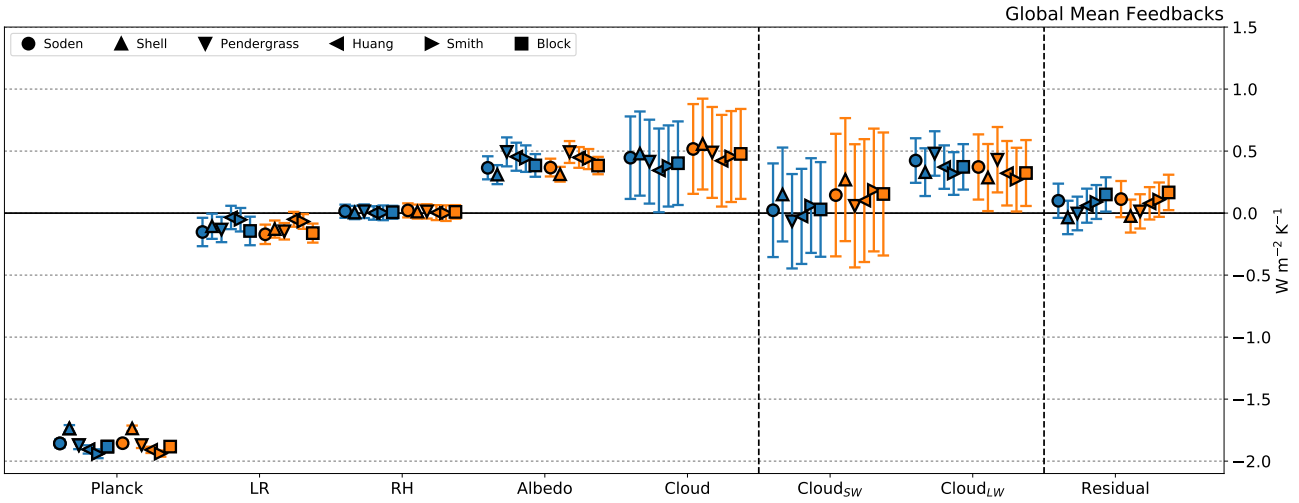

Figure S2. As in Figure 1C, but showing mean and across-model standard deviations of (blue) CMIP5 and (orange) CMIP6 feedbacks estimated with each of the six radiative kernels.

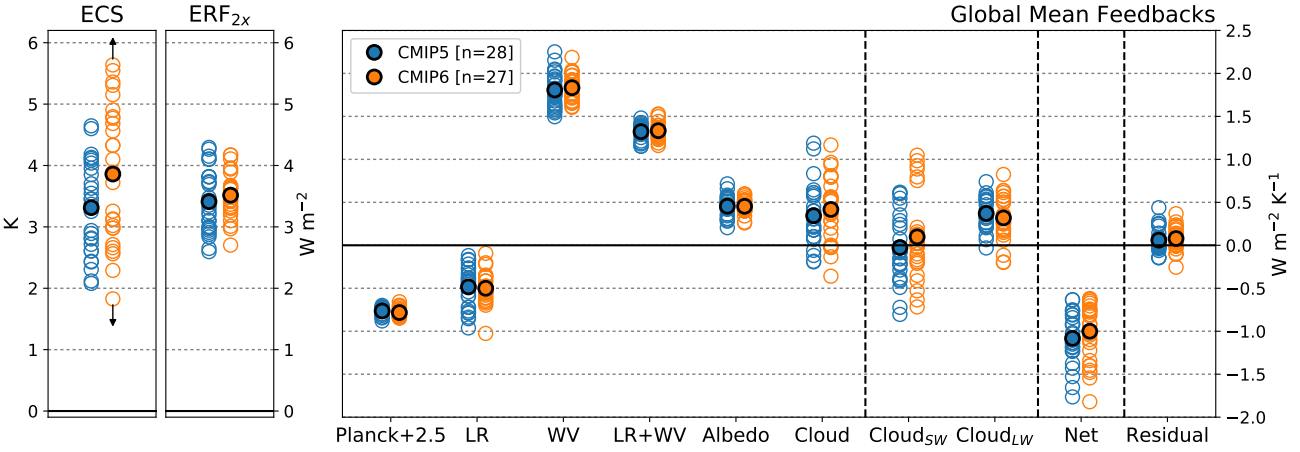

Figure S3. As in Figure 1A-C, but for the conventional feedback breakdown in which Planck and LR feedbacks are computed holding specific humidity fixed and the water vapor feedback quantifies the change in net TOA radiation due to temperature-mediated increases in specific humidity. Owing to their strong anti-correlation across models (Soden & Held, 2006), we also show the combined LR and WV feedbacks (LR+WV).

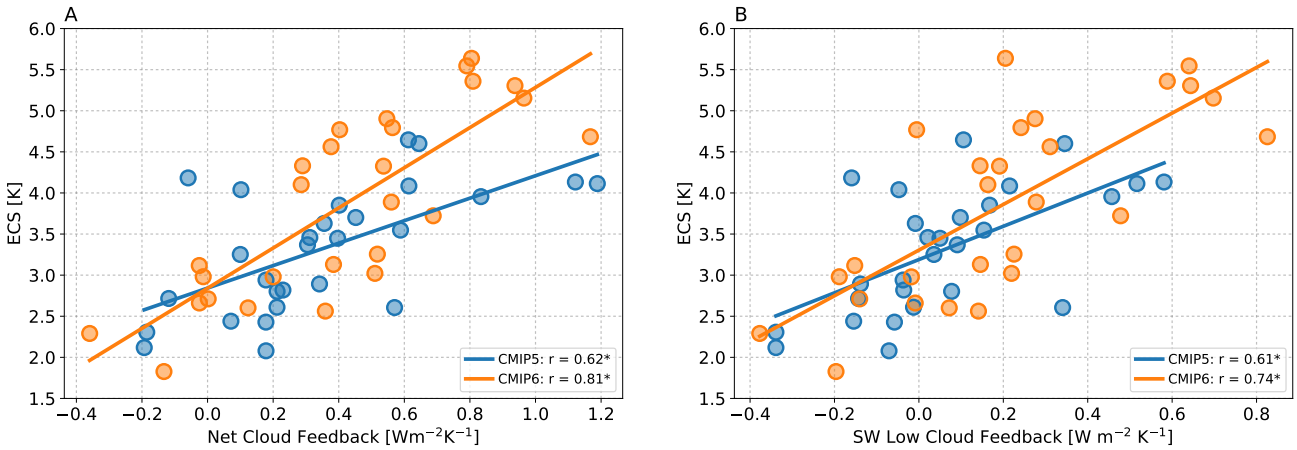

Figure S4. ECS plotted against (A) net cloud feedback and (B) SW low cloud feedback. Asterisks indicate statistically significant correlation coefficients at 95% confidence. Neither of the differences between CMIP5 and CMIP6 regression slopes is significant at 95% confidence.

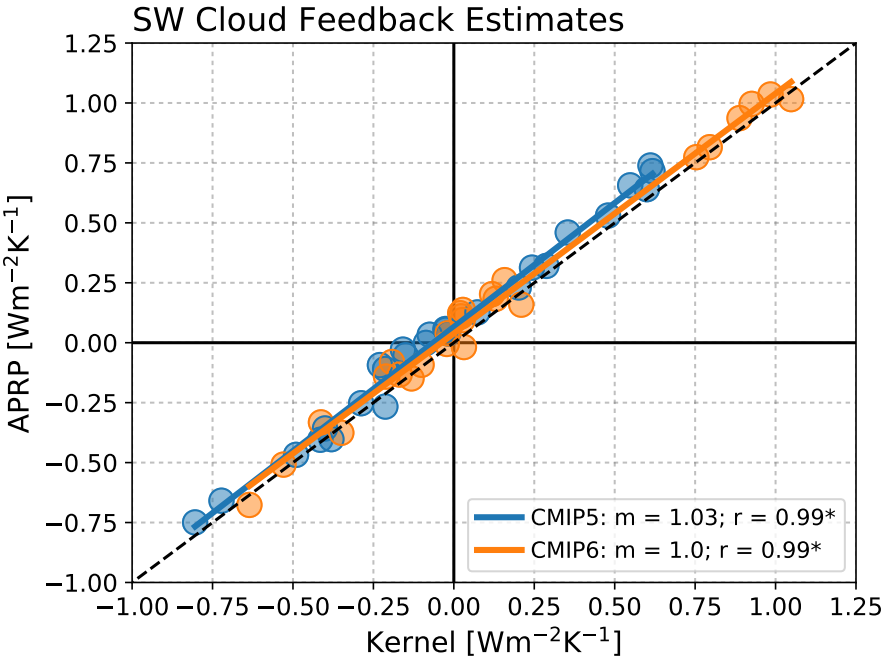

Figure S5. Global mean kernel-derived SW cloud feedbacks plotted against those derived using APRP for (blue) CMIP5 and (orange) CMIP6. Asterisks indicate statistically significant correlation coefficients at 95% confidence.

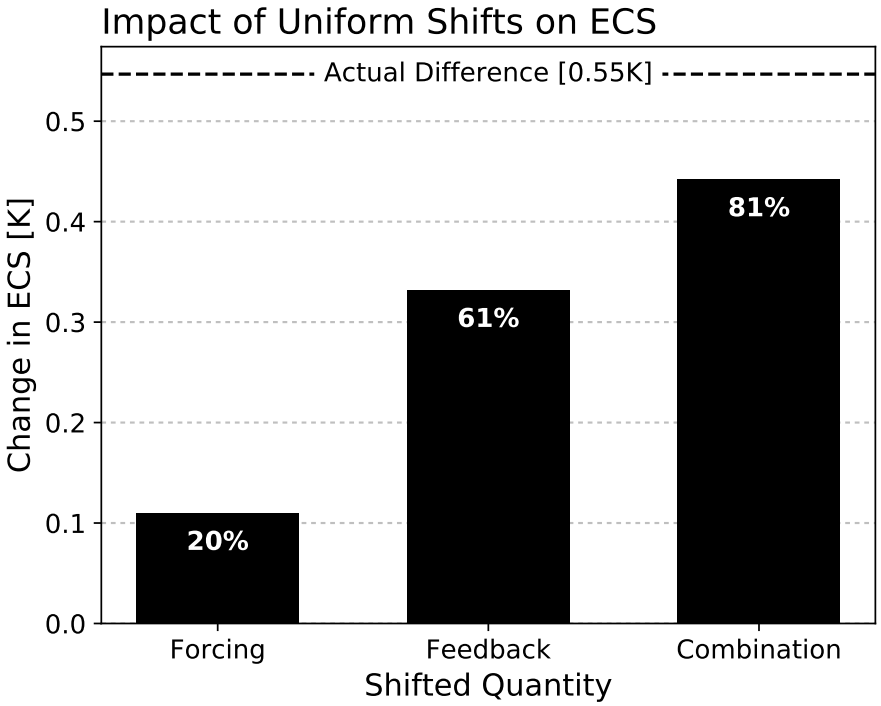

Figure S6. Changes in multi-model mean ECS due to hypothetical uniform shifts of forcing holding all else fixed, feedback holding all else fixed, and the combination of forcing and feedback holding all else fixed. Imposed forcing and feedback shifts are equal to the difference in multi-model mean $ERF_{2\times}$ and λ, respectively, between CMIP5 and CMIP6. Shifts are performed separately for CMIP5 and CMIP6 and then averaged. The change in mean ECS expressed as a percentage of the actual CMIP5-to-CMIP6 change is printed in each bar.

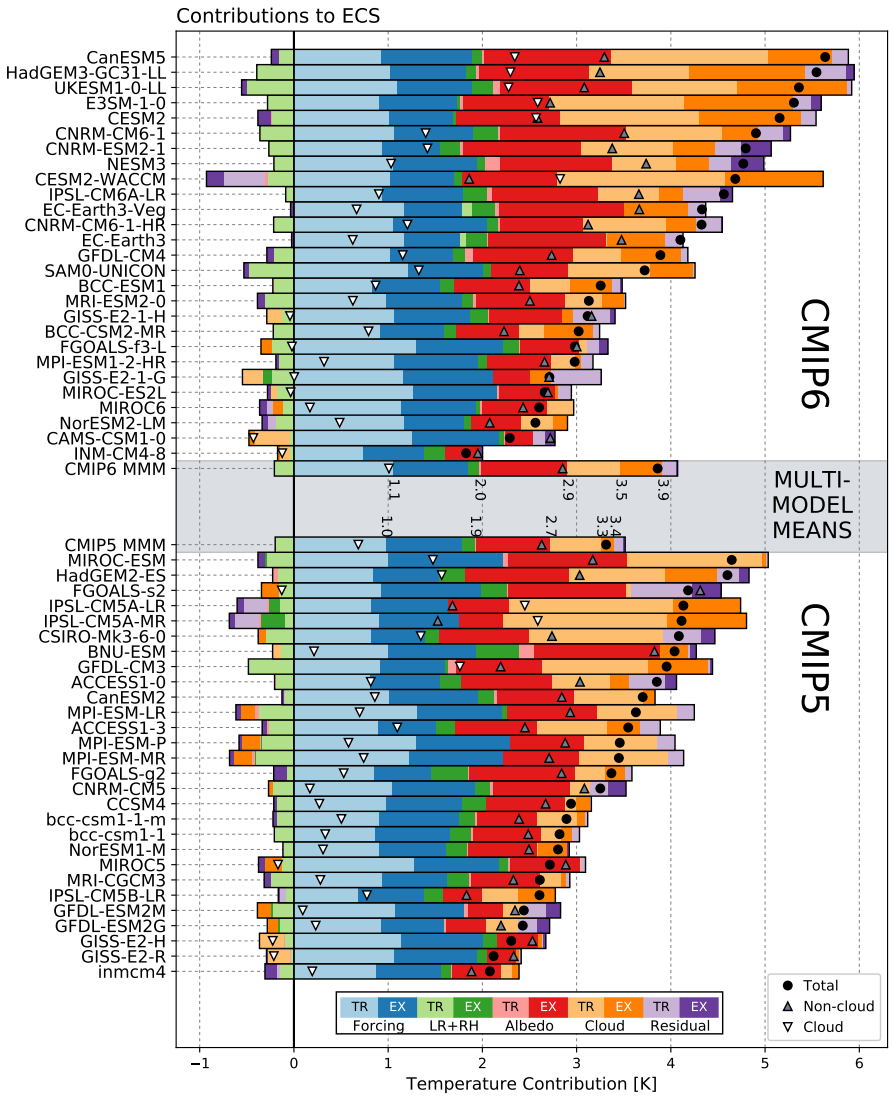

Figure S7. Contributions of forcing and feedbacks to ECS in each model and for the multi-model means. Contributions from the tropical and extratropical portion of the feedback are shown in light and dark shading, respectively. Black dots indicate the ECS in each model, while upward and downward pointing triangles indicate contributions from non-cloud and cloud feedbacks, respectively. Numbers printed next to the multi-model mean bars indicate the cumulative sum of each plotted component. Numerical values are not printed next to residual, extratropical forcing, and tropical albedo terms for clarity. Models within each collection are ordered by ECS.

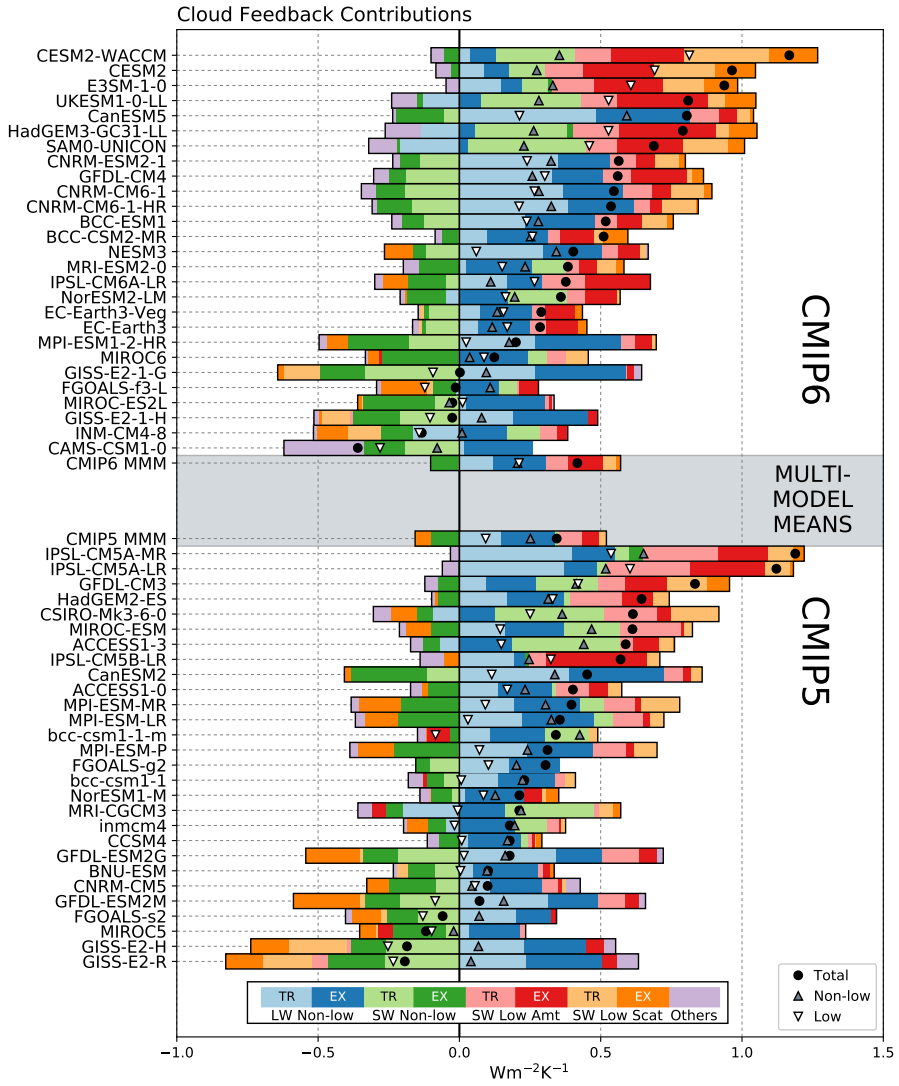

Figure S8. Cloud feedbacks due to low and non-low clouds in the (light shading) tropics and (dark shading) extratropics in each model and for the multi-model means. Non-low cloud feedbacks are separated into LW and SW components, and SW low cloud feedbacks are separated into amount and scattering components. "Others" represents the sum of LW low cloud feedbacks and the small difference between kernel- and APRP-derived SW low cloud feedback. Insufficient diagnostics are available to compute SW cloud amount and scattering feedbacks for the FGOALS-g2 and CAMS-CSM1-0 models. Black dots indicate the global mean net cloud feedback in each model, while upward and downward pointing triangles indicate total contributions from non-low and low clouds, respectively. Models within each collection are ordered by global mean net cloud feedback.

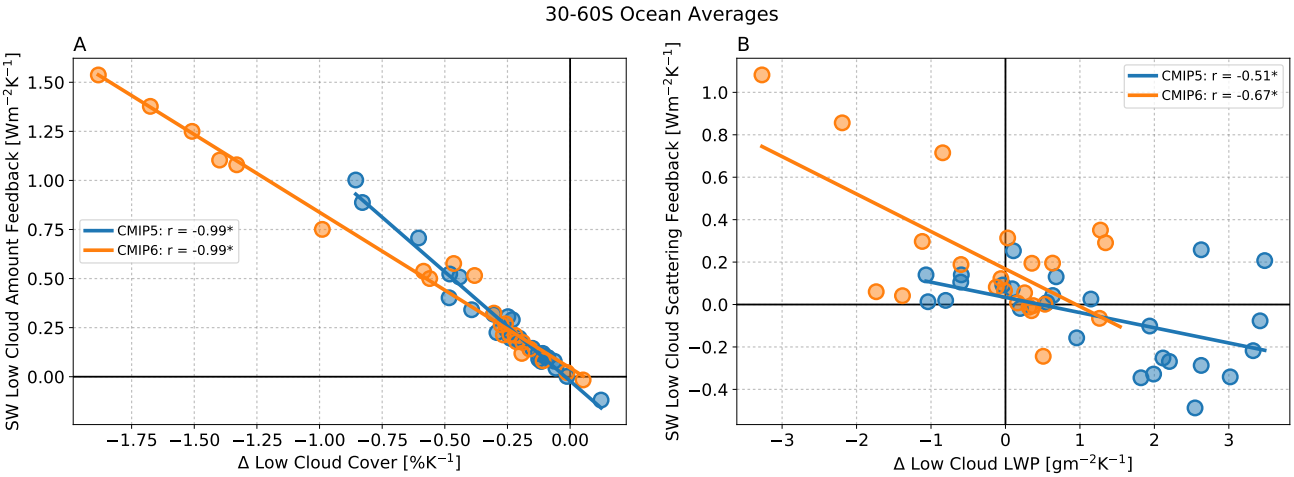

Figure S9. (A) SW low cloud amount feedback plotted against the change in low cloud cover. (B) SW low cloud scattering feedback plotted against the change in in-cloud liquid water path for low clouds. All quantities are marine averages over 30-60°S, with CMIP5 shown in blue and CMIP6 shown in orange. Asterisks indicate statistically significant correlation coefficients at 95% confidence.

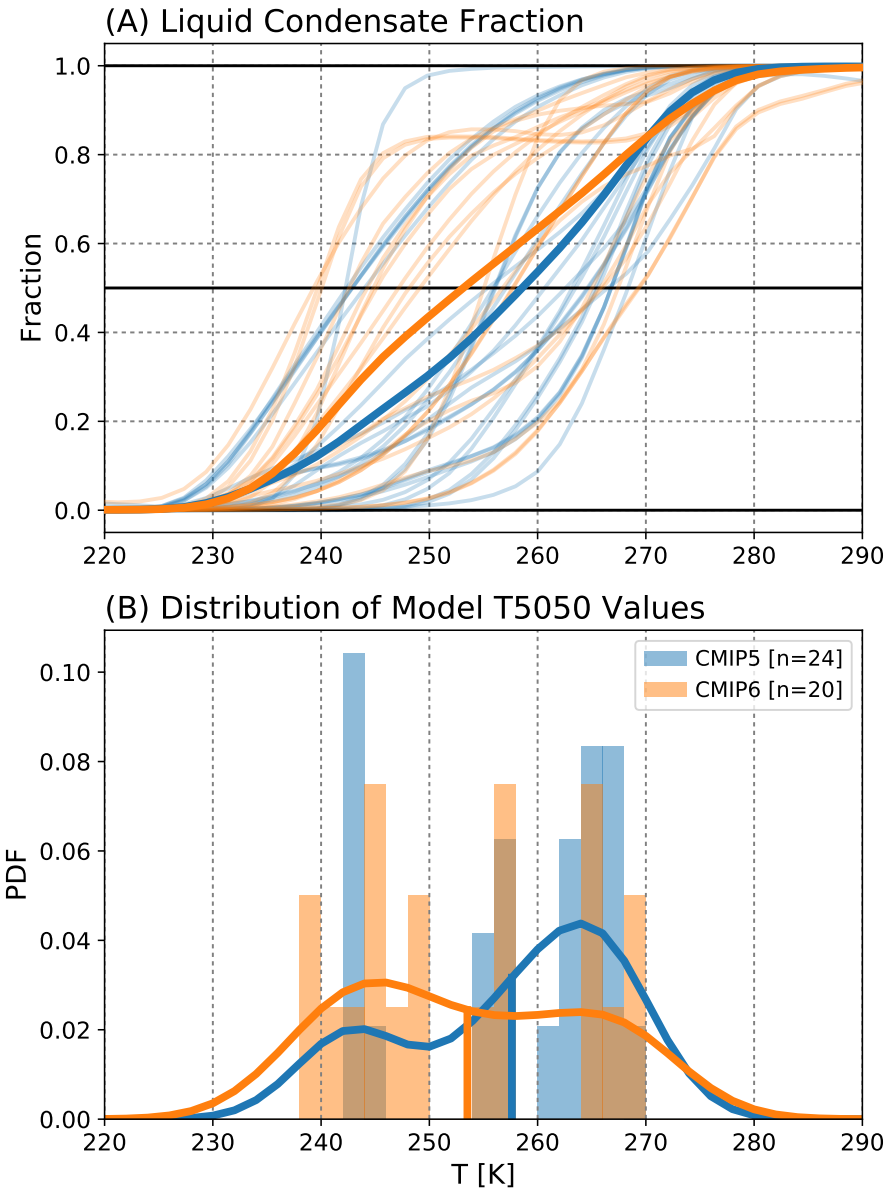

Figure S10. (A) Liquid condensate fraction (LCF) as a function of temperature for individual (blue) CMIP5 and (orange) CMIP6 models. LCF is defined as the ratio of liquid water path to total water path between 30 and 80 degrees latitude in both hemispheres. Multi-model means are indicated with thick lines. (B) Distribution of T5050 values (the temperatures at which LCF = 0.5) for CMIP5 and CMIP6 models, with kernel density estimates overlain. Multi-model means are indicated with vertical lines.

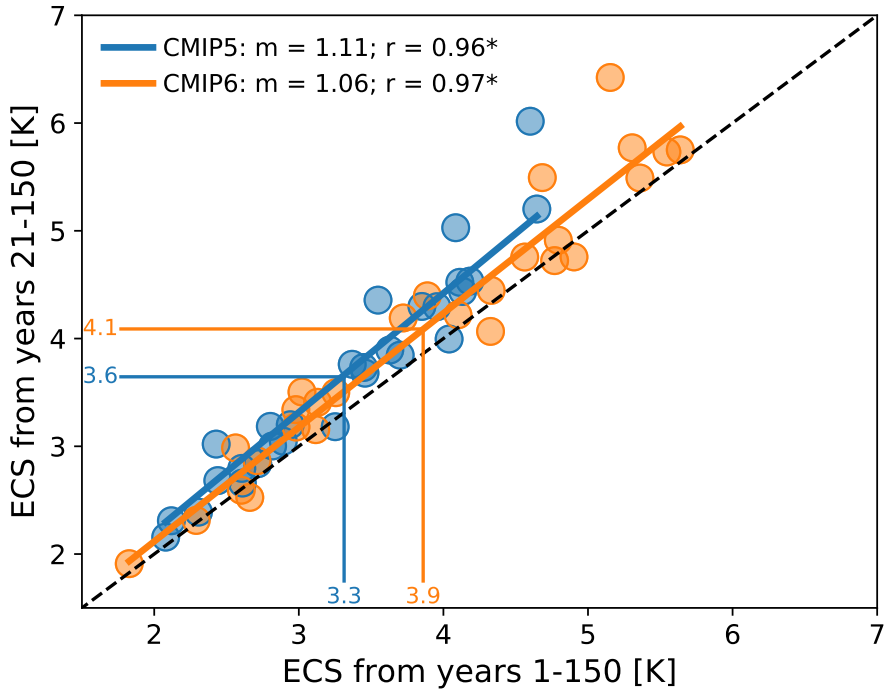

Figure S11. ECS estimated using all 150 annual anomalies from the abrupt-4xCO2 experiment plotted against ECS estimated using only the last 130 annual anomalies for (blue) CMIP5 and (orange) CMIP6 models. The dashed line indicates the 1:1 line, and solid lines extend to the multi-model average ECS values. The difference between CMIP5 and CMIP6 regression slopes is significant at 95% confidence.